

***Ab initio* calculations of the lattice dynamics of boron nitride nanotubes**

Ludger Wirtz and Angel Rubio

*Department of Material Physics, University of the Basque Country, Centro Mixto CSIC-UPV,  
and Donostia International Physics Center, Po. Manuel de Lardizabal 4, 20018 Donostia-San Sebastián, Spain*Raul Arenal de la Concha and Annick Loiseau  
*LEM, ONERA-CNRS, BP72, 92322 Châtillon Cedex, France*

(Received 24 March 2003; published 30 July 2003)

We present an extensive first-principles study of the phonons in boron nitride nanotubes using density functional perturbation theory in the local density approximation. Based on the nonsymmorphic rod-group symmetry of the tubes, the Raman- and infrared-active modes at the  $\Gamma$  point of the one-dimensional Brillouin zone are evaluated. For zigzag and chiral nanotubes, the set of infrared-active modes is a subset of the Raman-active modes. In particular, the radial breathing mode is not only Raman but also infrared active. However, for armchair tubes, the sets of infrared- and Raman-active modes are disjoint. This may serve to spectroscopically distinguish between macroscopic samples of zigzag-chiral and armchair nanotubes. We present the frequencies of the active modes of zigzag, chiral, and armchair tubes as a function of the tube diameter and compare the results with the frequencies obtained by the zone-folding method, i.e., the rolling of a single hexagonal BN sheet into a tube. Except for the high-frequency tangential modes, the zone-folding results are in very good agreement with the *ab initio* calculations. The radial breathing mode frequency can be derived by folding a sheet of *finite* width. Finally, we show that the effects of bundling on the phonon frequencies are small. This demonstrates that the obtained results for isolated BN tubes may serve as a basis for an accurate assignment of phonon modes in spectroscopic measurements.

DOI: 10.1103/PhysRevB.68.045425

PACS number(s): 78.20.Bh, 63.22.+m, 61.48.+c, 78.30.-j

**I. INTRODUCTION**

Besides carbon nanotubes<sup>1</sup> which are a promising material due to both their mechanical strength and their interesting electronic properties,<sup>2,3</sup> boron nitride (BN) tubes have recently attracted increased attention. Their stability was first predicted based on tight-binding<sup>4</sup> and first-principles<sup>5</sup> calculations, and shortly afterwards, their synthesis was achieved.<sup>6</sup> Meanwhile, production of BN tubes has been reported by different groups around the world.<sup>7-13</sup> Recently, the fabrication of single-wall BN tubes in gram quantities has been achieved.<sup>14</sup>

In contrast to C nanotubes which can be either semiconducting or metallic, depending on the chirality of the tube, BN nanotubes are always semiconducting with a large band gap of about 5.5 eV. Density functional theory (DFT) calculations and quasi particle calculations have shown that this gap is nearly independent of the tube diameter, chirality, and whether the nanotube is single walled, multiwalled, or packed in bundles.<sup>4,5</sup> [The DFT band gap is pinned at the constant value of about 4 eV whereas self-energy corrections to the quasiparticle energies open the gap to 5.5 eV (Ref. 15)]. A structural difference between BN and C tubes is that for tubes with small diameter, the BN system buckles with the B atoms moving inward and the N atoms outward.<sup>5</sup> This results in a dipolar double cylinder shell structure, which combined with the fact that BN tubes exhibit quantum polarization effects<sup>16</sup> makes them attractive for electromechanical applications and as piezoelectrics. The uniform electronic properties suggest that BN nanotubes may have significant advantages for applications in electronic and mechanical devices. Furthermore, the bottom of the conduction band is a

nearly free-electron-like state. This state remains the bottom of the conduction band even in the multiwall case and, in the case of *n*-type doping, will play an important role for potential applications in field emission devices and molecular transport.<sup>17</sup>

Raman and infrared (IR) spectroscopy in which phonons are excited by inelastic scattering of light or light absorption, respectively, are convenient tools to investigate the composition of macroscopic samples of nanotubes. Early Raman<sup>18</sup> and infrared<sup>19</sup> investigations were performed on samples of multiwall carbon nanotubes (MWNT's) and showed signatures close to those of graphite. However, after the production of single-wall nanotubes (SWNT's) in large quantities, resonant Raman spectroscopy turned into a very precise, highly diameter selective identification tool.<sup>20</sup> Especially the low-frequency Raman modes such as the radial breathing mode (RBM) strongly depend on the tube diameter and facilitate identification. The high-frequency modes are only weakly diameter dependent, but their intensity in the resonant Raman spectra strongly depends on the diameter through the electronic excitation energy.<sup>21</sup> IR spectroscopy on SWNT's (Ref. 22) shows only small differences when compared to IR data of graphite. For BN nanotubes, the situation is quite different: The Raman intensities in the visible light frequencies are weaker than for C nanotubes, since the Raman scattering is nonresonant due to the wide band gap.<sup>23</sup> On the other hand, BN is a polar material and shows a much higher IR absorbance than C nanotubes.<sup>23,24</sup> It is expected that the combination of Raman and IR spectroscopy will develop into a standard characterization tool for BN tubes such as it is already in the case of C tubes. At this stage it is very important to have a detailed knowledge of phonon fre-

quencies in BN nanotubes and to understand the dependence on diameter and chirality, in order to guide future experiments. This is the goal of the present work where for the first time reliable *ab initio* phonon calculations are presented for BN nanotubes.

For graphite and carbon nanotubes, many calculations of phonons have been performed using the force constant approach<sup>2,25</sup> where interatomic force constants up to fourth-nearest-neighbor interaction have been fitted to experimental data. This approach is very fast and, in combination with the zone-folding method<sup>2</sup> (i.e., the construction of phonons in the tube from the phonons of a sheet which is rolled up to form the tube), allows a good intuitive understanding of phonons in nanotubes. However, *ab initio* calculations of the phonon dispersion relation of graphite<sup>26–28</sup> using DFT display a deviation of up to 200 cm<sup>−1</sup> from the dispersion relation obtained with the force constants of Ref. 25 while being in good agreement<sup>26,27</sup> with experimental data. Going beyond the force constant approach, phonons in carbon nanotubes have been calculated using tight-binding techniques,<sup>29</sup> DFT with a localized-orbital approach,<sup>30,31</sup> and DFT calculations employing plane waves<sup>28,32,33</sup> which are the most accurate calculations up to date. For this reason, in a recent joint experimental and theoretical study of Raman and IR spectra of single-wall BN nanotubes,<sup>23</sup> we have employed this method to calculate phonons for a reliable discussion of the observed peaks. In this paper, we present a detailed account of the calculations and the theoretical results. Phonons in BN nanotubes have also been calculated by a tight-binding technique<sup>34</sup> and by a valence-shell model of the lattice dynamics.<sup>35</sup> The tight-binding results lack predictive power as they show important differences in the high- and medium-frequency regimes of the dispersion relation of the single sheet when compared with experiment and with earlier *ab initio* calculations of hexagonal BN.<sup>36</sup> However, the valence-shell model, as its parameters are fitted to the data on *h*-BN, reproduces rather well the phonons of the tubes.

Section II describes the method of calculation. The equilibrium geometry of the tubes is discussed in Sec. III. In Sec. IV we present the dispersion relation of the hexagonal BN sheet and of BN tubes and discuss the characteristic differences with respect to the graphene sheet and C nanotubes. In Sec. V we review the symmetry analysis of the Raman- and infrared-active modes at the  $\Gamma$  point. In Sec. VI we explain how the symmetry assignment can be intuitively understood by the zone-folding method. In Sec. VII we present the main results of this paper, the frequencies of active modes in zigzag, chiral, and armchair tubes as a function of tube diameter. Finally, Sec. VIII discusses how the phonon frequencies are influenced by packing the tubes into bundles. The Appendix discusses the deviation of the zone-folding procedure from the *ab initio* results for the low phonon frequencies and presents a derivation for the frequency of the radial breathing mode by folding a sheet of finite width.

## II. METHOD

The calculations have been performed with the code ABINIT (Ref. 37) using DFT (Ref. 38) in the local density ap-

proximation (LDA) (Ref. 39). We employ Troullier-Martins pseudopotentials<sup>40</sup> and a plane-wave basis set with an energy cutoff at 80 Ry. The (infinitely long) BN tubes are periodic along the tube axis ( $z$  direction). Since the use of a plane-wave expansion requires periodic supercells in all three dimensions, we calculate effectively a triangular periodic array of nanotubes. In order to keep the effect of intertube interactions low, we use a closest distance of 7.4 Å between the tubes. In a first step, the tube geometry is optimized until the forces acting on all atoms are smaller than  $2.5 \times 10^{-3}$  eV/Å. At the same time, the stress along the tube axis is minimized by optimizing the unit-cell size in the  $z$  direction. The resulting tube geometry is discussed in Sec. III.

The phonon frequencies  $\omega$  as a function of the phonon wave vector  $q$  are the solution of the secular equation

$$\det \left| \frac{1}{\sqrt{M_s M_t}} C_{st}^{\alpha\beta}(q) - \omega^2(q) \right| = 0. \quad (2.1)$$

$M_s$  and  $M_t$  denote the atomic masses of atoms  $s$  and  $t$  and the dynamical matrix is defined as

$$C_{st}^{\alpha\beta}(q) = \frac{\partial^2 E}{\partial u_s^{\alpha}(q) \partial u_t^{\beta}(q)}, \quad (2.2)$$

where  $u_s^{\alpha}$  denotes the displacement of atom  $s$  in direction  $\alpha$ . The dynamical matrix can be calculated by displacing the atoms of the unit cell into all three directions, performing an energy calculation of the perturbed geometry and calculating the second derivatives in Eq. (2.2) by a finite-difference method. This way has been chosen in the phonon calculations of Ref. 28 for carbon nanotubes. In our calculations, we treat the atomic displacement as a perturbation of the equilibrium geometry and use density functional perturbation theory (DFPT) (Ref. 41) as implemented in ABINIT (Ref. 42) for the calculation of the dynamical matrix. Since the space-group symmetry of a periodic array of nanotubes does not reflect the helical symmetry of isolated BN nanotubes, in principle, each atom of the unit cell has to be displaced in all three directions. However, if the distance between the tubes is large enough such that they are quasi-isolated, it is sufficient to displace only the symmetry-inequivalent atoms of the unit cell. The residual elements of the dynamical matrix are obtained by application of the appropriate symmetry transformations. Thus, in carbon nanotubes, only the displacements of one atom need to be calculated,<sup>28,43</sup> and in BN tubes the displacements of two atoms (one B and one N) have to be calculated. For BN tubes, this symmetrization only works if a sufficiently large intertube distance (7.4 Å) is used, because a smaller intertube distance leads to artificial deformations from the cylindrical geometry of the tube.<sup>44</sup>

We used a  $10 \times 10$  Monkhorst-Pack  $k$ -point sampling of the first two-dimensional (2D) Brillouin zone (BZ) for the BN sheet (corresponding to a  $10 \times 10 \times 1$  grid in the 3D BZ of the periodic supercell with an intersheet distance of 7.3 Å). For the 1D BZ of armchair (zigzag) BN tubes, 10 (6) points were used, corresponding to 5 (3) irreducible  $k$  points. We have checked that this set of  $k$  points and energy cutoff at

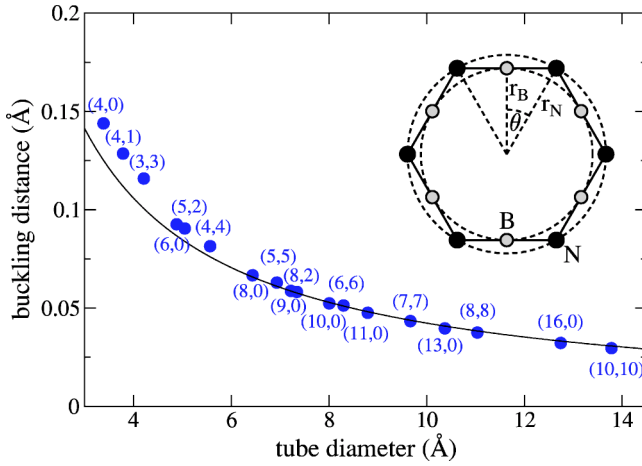


FIG. 1. Buckling distance in BN single-wall nanotubes as a function of tube diameter.

80 Ry leads to phonon frequencies converged to within  $4 \text{ cm}^{-1}$ . Since hexagonal BN and BN tubes are wide-band-gap insulators with relatively flat bands, considerably fewer  $k$  points are needed to reach convergence for BN than for graphite and carbon nanotubes. The proper description of all phonon modes in metallic C nanotubes requires a much larger  $k$ -point sampling due to the subtle opening of an electronic band gap for certain phononic displacements.<sup>33</sup>

Since  $h$ -BN is a polar material where N is slightly negatively charged and B slightly positively, the long-range character of the Coulomb potential gives rise to a macroscopic electric field  $E$  for longitudinal optical phonons in the limit  $q \rightarrow 0$ . This gives rise to a splitting (LO-TO splitting) between the longitudinal and transverse optical modes which amounts to about  $200 \text{ cm}^{-1}$  at the  $\Gamma$  point.<sup>36</sup> In order to properly account for this effect, the dynamical matrix [Eq. (2.2)] must be corrected under inclusion of the Born effective charge tensor  $Z_s^{*\alpha\beta}$  of the ions and the static dielectric tensor  $\epsilon_\infty^{\alpha\beta}$ . Both quantities can be calculated in DFPT (Refs. 41 and 42) from the macroscopic electric polarization  $P$  of the medium. For a densely packed periodic array of tubes, a similar splitting is expected and can indeed be observed.<sup>45</sup> However, this effect is restricted to three-dimensional (infinitely extended) systems. In this article we are dealing with the frequencies of isolated tubes or small bundles of tubes. As long as the diameter of the nanotube bundles is smaller than the wavelength of the laser light, the system is effectively one dimensional and no LO-TO splitting takes place.

### III. EQUILIBRIUM GEOMETRY

The calculation of phonons starts with a determination of the optimized tube geometry by minimizing both stress and Hellmann-Feynman forces. Minimization of the stress in the sheet leads to a BN bond length of  $1.44 \text{ Å}$  which is close to the literature value of  $1.45 \text{ Å}$  for bulk  $h$ -BN.<sup>46</sup> It was already noted in the first LDA studies of BN tubes<sup>5</sup> that the boron-nitrogen bonds display a buckling with the nitrogen atoms moving slightly outwards and the boron atoms moving slightly inwards (see inset of Fig. 1). This leads to the for-

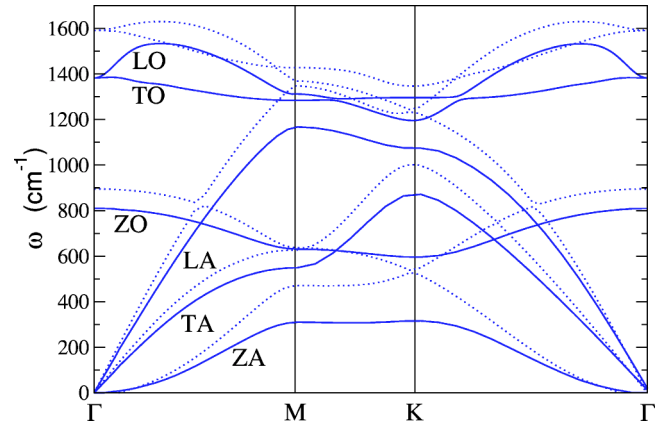


FIG. 2. Calculated phonon dispersion relation of the single hexagonal BN sheet (solid lines) in comparison with graphene (dotted lines).

mation of a negative outer N cylinder and a positive inner B cylinder. Figure 1 shows that the buckling distance between these two cylinders is to a very good approximation inversely proportional to the tube diameter (except for the tubes with very small diameters where the decrease is faster). In Ref. 5 it was described that the threefold-coordinated (and slightly positively charged) boron atoms have the tendency to keep the planar  $sp^2$  bonding geometry with bond angles of  $120^\circ$  while the (slightly negatively charged) nitrogen atoms are more susceptible to an admixture of  $sp^3$  hybridization leading to smaller bond angles. With this hypothesis, a very simple explanation of the  $1/r$  dependence can be given. The inset of Fig. 1 shows a two-dimensional projection of the buckled geometry for a  $(n,0)$  zigzag tube. The nitrogen atoms are located at the corners of the polygon with distance  $r_N$  from the center. The boron atoms are accordingly placed at the midpoints of the sides of the polygon. The angle  $\theta$  is inversely proportional to  $n$  and thereby to the tube radius  $r$ . Therefore, also the buckling distance is inversely proportional to the radius:  $r_N - r_B = r - r \cos \theta \approx r - r(1 - \frac{1}{2}\theta^2) \propto 1/r$ . For smaller tube radii ( $D = 2r < 7 \text{ Å}$ ) the strain energy due to the curvature of the tube (see Ref. 5) becomes so large that the boron atoms no longer keep their planar bonding geometry but also acquire an admixture of  $sp^3$  hybridization.

### IV. PHONON DISPERSION RELATIONS

We start the presentation of phonons with the calculated phonon dispersion relation of the hexagonal BN sheet in Fig. 2. Through the zone-folding procedure this gives a good quantitative estimate for the phonon frequencies in the tubes. For comparison we have added with dotted lines the phonon dispersion relation of the graphene sheet. The latter one is in almost perfect agreement with the recent calculation of Dubay and Kresse.<sup>28,47</sup> In general, the phonons of the BN sheet are considerably softer than the phonons of the graphene sheet which is related to the fact that the elastic constants of  $h$ -BN are smaller than the ones of graphite. Furthermore, the degeneracy of the out-of-plane acoustic and optical (ZA and ZO) modes and the degeneracy of the longitudinal acoustic and optical (LA and LO) modes in



graphene is lifted in BN due to the different masses of B and N. As discussed in Ref. 28, the agreement between theory and experimental data on phonons in graphite<sup>50,51</sup> is very good except for the LA branch at the  $M$  point which seems too low by about  $200 \text{ cm}^{-1}$ . The origin of this discrepancy is not yet clear and needs to be revisited both experimentally and theoretically. We note, therefore, that a similar discrepancy could occur for the BN sheet at the  $M$  point. Due to the difficulty of producing high-quality crystals of  $h$ -BN, experimental data on the phonon-dispersion relation is so far only available for a monolayer of  $h$ -BN on a metal substrate,<sup>52</sup> giving rise to strong deviations from the theoretical phonon dispersion relation.<sup>36</sup>

The phonon dispersion relation of the sheet follows very closely the *ab initio* calculated dispersion relation of bulk hexagonal BN (Ref. 36) when one subtracts the phonon branches that are influenced by the interplane interaction. This is analogous to the comparison of phonon dispersion relations in the graphene sheet<sup>28</sup> and in bulk graphite<sup>26,27</sup> and due to the fact that the intersheet interaction is much weaker than the interaction between atoms within the sheet. However, in contrast to the nonpolar graphite, BN is a polar substance with a long-range dipole-dipole interaction between the sheets. This leads to a splitting between the longitudinal and transverse optical mode (LO-TO splitting) at the  $\Gamma$  point with the LO mode being higher in energy due to its coupling to a self-induced homogeneous electric field. Therefore, the dispersion relation of bulk hexagonal BN (Fig. 3 of Ref. 36) displays two LO modes; the lower branch shows a strong overbending in the direction  $M \rightarrow \Gamma$  but is degenerate with one of the TO branches at  $\Gamma$ . This is the branch which corresponds to an oscillation with a phase difference of  $\pi$  between nearest-neighbor planes. The higher LO branch for which neighboring planes oscillate in phase displays a splitting of more than  $200 \text{ cm}^{-1}$  with respect to the corresponding TO mode at  $\Gamma$ .

As pointed out in Refs. 16 and 34, the effect of LO-TO splitting should be absent in a two-dimensional single sheet. Since we use a plane-wave DFT code, however, we cannot calculate a really isolated sheet of BN, but only a “bulk” system with enlarged intersheet distance. We have observed that the corresponding artificial LO-TO splitting decreases with the intersheet distance, but still amounts to  $180 \text{ cm}^{-1}$  at an intersheet distance of  $d_z = 7.3 \text{ \AA}$  which is about twice the equilibrium distance of hexagonal BN and a distance where the “chemical” interaction that would arise from the overlap of wave functions of neighboring sheets has long faded out. In order to simulate an isolated sheet, we have therefore applied a computational trick for the LO branch: We calculate the dispersion using a  $z$  component of the phonon wave vector  $q_z = \pi/d_z$  where two neighboring sheets oscillate out of phase and the dipoles created in a unit cell through atomic displacement are exactly canceled out through the opposite dipole in a neighboring sheet. In this way, the interplane electrostatic interaction decreases much faster and at  $d_z = 7.3 \text{ \AA}$ , the phonon frequencies of the LO branch have already converged to an estimated value of  $10 \text{ cm}^{-1}$  from the isolated sheet. The resulting LO branch in Fig. 2 displays an overbending which is not only much stronger than the over-

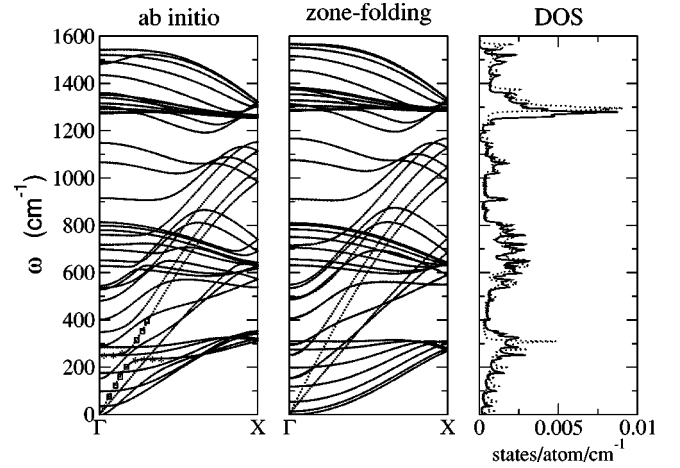


FIG. 3. Calculated phonon dispersion relation and density of states (DOS) in the (6,6) armchair BN nanotube. We compare the results of *ab initio* calculations with the zone-folding method (see text for details). In the right panel the solid line is the *ab initio* DOS and the dotted line the zone-folding DOS. The symbols in the left panel indicate the avoided crossing between the RBM (asterisks) and the longitudinal acoustic mode (boxes).

bending in the graphene sheet, but also more pronounced (and with a maximum closer to  $\Gamma$ ) than the corresponding LO branch of hexagonal BN. Also, the overbending is more pronounced than in the calculation of the sheet dispersion relation by Miyamoto *et al.*<sup>53</sup> who used DFT employing a periodic supercell.

In Fig. 3 we compare the *ab initio* phonon dispersion relation of a (6,6) BN nanotube with the corresponding zone-folding dispersion relation. The zone-folding method works equally good as in the case of carbon nanotubes.<sup>28</sup> Here and there, the major difference lies in the low-frequency part of the spectrum and is due to the coupling of in-plane and out-of-plane modes of the sheet upon rolling into a tube. This leads to a stiffening of the low-frequency tube modes. Another pronounced difference is the avoided crossings in the *ab initio* dispersion relation. According to the noncrossing rule of von Neumann and Wigner,<sup>54</sup> energy levels of modes which have the same symmetry do not cross when an adiabatic parameter (in this case the phonon wave vector  $q$ ) is changed. A prime example is the longitudinal optical mode (marked by boxes) which starts from zero frequency at the  $\Gamma$  point with the same slope as the LA mode of the sheet (compare Fig. 2) and displays a clear avoided crossing with the radial breathing mode [ $\omega(k=0) = 251 \text{ cm}^{-1}$ , marked by asterisks] at  $k \approx 0.2\pi/T$ . Both modes have  $A_1$  symmetry at the  $\Gamma$  point (see next section). Note that the “adiabatic” dispersion curve of the RBM is nearly planar in  $q$  over a wide range of the Brillouin zone. This is independent of chirality (we observed the same behavior in the dispersion of zigzag tubes) and can also be seen in the dispersion relations of Ref. 28 for carbon tubes.

A more detailed analysis of the zone-folding of Raman- and infrared-active modes follows in Sec. VI and in the Appendix. In general, the zone-folding method not only reproduces quite well the dispersion relation, but also yields a good estimate of the total phonon density of states, even

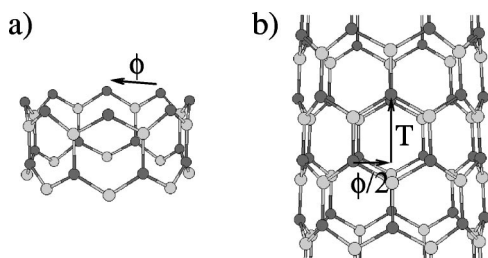


FIG. 4. Comparison of the point-group symmetry of the unit cell with the space-group symmetry of zigzag BN tubes.

though some systematic deviation towards higher phonon frequencies is clearly visible in the right panel of Fig. 3.

## V. SYMMETRY ANALYSIS

In Raman and IR spectroscopy, only phonons at (or close to) the  $\Gamma$  point of the one-dimensional Brillouin zone can be excited (as long as we restrict our discussion to first-order processes). Furthermore, in Raman spectroscopy, only modes that transform under symmetry operations as a quadratic form are active, in IR spectroscopy only modes that transform as a vector.<sup>55</sup> For (infinitely extended) systems with translational symmetry, the “point group in the space group” determines through the selection rules which modes are active and which are not. In quasi-one-dimensional systems with translational symmetry, it is accordingly the “point group in the rod group” that has to be evaluated. This was done recently by Damnjanović *et al.*<sup>56</sup> and by Alon<sup>57</sup> for C nanotubes and BN nanotubes.<sup>58</sup> Figure 4 summarizes the findings for BN tubes: It can be easily seen that the unit cell of a  $(n,0)$  zigzag tube possesses an  $n$ -fold rotation axis (with rotation angle  $\phi = 2\pi/n$ ). In addition,  $n$  (indeed, even  $2n$ ) vertical reflection-symmetry planes (containing the tube axis) can be found. Thus the unit cell of a zigzag tube transforms under the  $C_{nv}$  symmetry group. In the infinitely extended tube, the operations of the  $C_{nv}$  point group are valid as well, but—in addition—a rotation by  $\phi/2$  with subsequent translation by  $T/2$  also maps the system onto itself. This leads to the conclusion that for the infinitely extended system, the  $C_{2nv}$  symmetry group is the relevant one for symmetry analysis of Raman- and IR-active modes. Analogously, for  $(n,n)$  armchair tubes, the symmetry group of the unit cell is  $C_{nh}$  and the symmetry group of the infinitely extended tube is  $C_{2nh}$ . Finally, for chiral  $(n,m)$  tubes, the unit cell has the low point-group symmetry  $C_d$ , where  $d$  is the greatest common divisor of  $n$  and  $m$ . However, the infinitely extended tube is described by the  $C_N$  symmetry group, where  $N$  is the number of hexagons ( $=2$  times the number of atoms) per unit cell which is, in general, much larger than  $d$ .

The number of active modes is found by determining how often each irreducible representation appears in the (reducible) representation of the symmetry group ( $C_{2nv}$ ,  $C_{2nh}$ , or  $C_N$ , respectively) which is given by the  $12n$  vibrational degrees of freedom of the unit cell. For zigzag tubes this leads to 14 Raman-active modes<sup>58</sup> (3 with  $A_1$  symmetry, 5 with  $E_1$  symmetry, and 6 with  $E_2$  symmetry, where the  $E_1$  and the  $A_1$  modes with vanishing frequency have already been sub-

tracted). Out of these modes, 8 modes ( $3A_1$  and  $5E_1$ ) are also IR active. In the case of chiral tubes, there are 15 Raman active modes ( $4A$ ,  $5E_1$ , and  $6E_2$ ) out of which 9 modes ( $4A$  and  $5E_1$ ) are also IR active. The small difference in the number of active modes between zigzag and chiral tubes stems from the fact that the additional vertical reflection symmetry of the zigzag tube causes a distinction between Raman+IR active  $A_1$  modes and nonactive  $A_2$  modes. The sets of Raman- and IR-active modes for BN armchair tubes are disjoint: 9 modes are Raman active (3 with  $A_g$  symmetry, 2 with  $E_{1g}$  symmetry, and 4 with  $E_{2g}$  symmetry) and 4 modes are IR active (1 with  $A_u$  symmetry and 3 with  $E_{1u}$  symmetry).<sup>59</sup> In the next section, it will be explained how these modes can be constructed from the modes at or close to the  $\Gamma$  point in the BN sheet.

Under certain experimental conditions, if the tubes are short compared to the wavelength of the scattered laser light, the tubes are expected to display the spectroscopic properties of very large molecules rather than of infinitely extended systems (finite-size effect). The BN tubes that were recently investigated by IR and Raman spectroscopy had a typical length between 100 nm and 400 nm,<sup>23</sup> i.e., of the order of the wavelength of visible light and definitely shorter than the wavelength of infrared light. These tubes are indeed long enough such that the phonon frequencies correspond to the frequencies of infinitely extended systems. However, for the evaluation of active modes, the point group of the “molecule” should be used. Assuming that the closing caps at the tube ends are constructed such that they do not further reduce the symmetry of the system, the point group of the finite zigzag tube is  $C_{nv}$ , coinciding with the point group of the unit cell. The symmetry of the finite armchair tubes can be either  $C_{nh}$  or  $S_{2n}$ . Finite-length chiral tubes have either no point group symmetry or a very low  $n$ -fold rotation axis, depending on the rotation symmetry of the unit cell.

Due to the relaxation of symmetry constraints, additional active modes may show up in the spectra. For zigzag tubes, 16 additional modes ( $4A_1$ ,  $6E_1$ , and  $6E_2$ ) are Raman active, out of which 10 ( $4A_1$  and  $6E_1$ ) correspond to modes that are also IR active. For armchair tubes (assuming  $C_{nh}$  symmetry), 10 additional modes ( $4A_g$ ,  $2E_{1g}$ , and  $4E_{2g}$ ) are Raman active and 6 additional modes are IR active ( $2A_u$  and  $4E_{1u}$ ).<sup>60</sup> In the zone-folding picture, these additional modes correspond to modes at or close to the  $M$  point in the BN sheet. In chiral tubes, if the unit cell does not have any symmetry, all modes can, in principle, be Raman and IR active. However, the intensity of most of the modes may be very weak and decreases with increasing tube length. We note that the reduced symmetry of finite-length tubes does not influence the fact that Raman- and IR-active modes are disjoint for armchair tubes and for zigzag and chiral tubes the IR-active modes are a subset of the Raman-active modes.

## VI. ZONE-FOLDING METHOD

In this section we review the zone-folding method which has been frequently used for the calculation of electronic band structure and phonons in C nanotubes<sup>2,3</sup> and demonstrate how the different Raman- and infrared-active modes

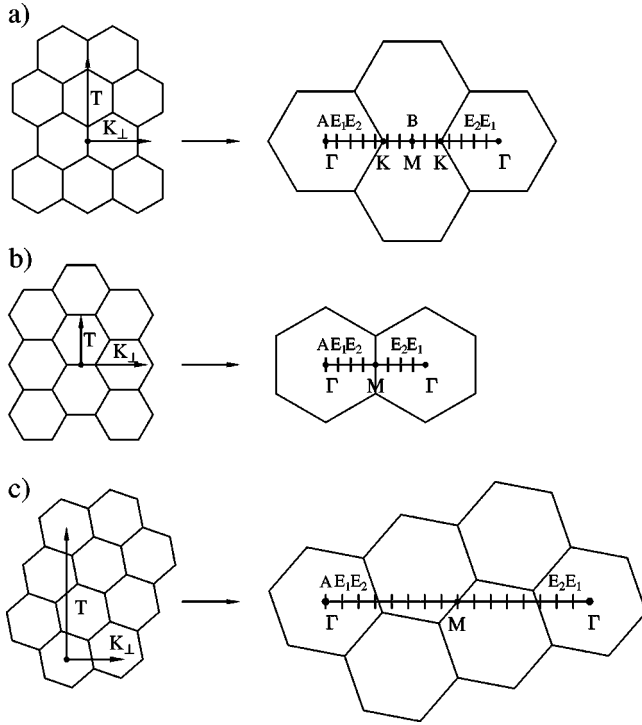


FIG. 5. Sketch of the zone-folding method (a) for  $(n,0)$  zigzag nanotubes, (b) for  $(n,n)$  armchair nanotubes, and (c) for  $(4n,n)$  chiral nanotubes. Left side: a hexagonal BN sheet is rolled in a perpendicular direction to the primitive translation vector  $\vec{T}$ . The component  $K_{\perp}$  of the phonon wave vector in the circumferential direction is quantized. Right side: in the two-dimensional Brillouin zone of zigzag nanotubes, the quantization corresponds to  $2n$  steps along the line  $\Gamma \rightarrow K \rightarrow M \rightarrow K \rightarrow \Gamma$ . In armchair nanotubes  $2n$  discrete steps are taken along the line  $\Gamma \rightarrow M \rightarrow \Gamma$ , while in chiral tubes the discretization proceeds along a line connecting more distant  $\Gamma$  points. The points at and close to  $\Gamma$  give rise to the Raman- and IR-active  $A$ ,  $E_1$ , and  $E_2$  modes.

can be deduced from it in the case of BN nanotubes. Thus, the symmetry analysis of the previous section can be understood in a pictorial way. Figure 5(a) demonstrates the scenario for  $(n,0)$  zigzag nanotubes. The sheet is rolled up such that the tube axis is parallel to the translation vector  $\vec{T}$  whose lengths corresponds to the lengths of the one-dimensional unit cell of the tube. The component  $K_{\perp}$  of the phonon wave vector  $\vec{K}$  which points into the circumferential direction of the tube is quantized. For zigzag nanotubes this means that in reciprocal space,  $K_{\perp}$  can assume  $2n$  discrete values ( $\mu = 0, \dots, 2n-1$ ) along the line  $\Gamma \rightarrow K \rightarrow M \rightarrow K \rightarrow \Gamma$ . The parallel component  $K_{\parallel}$  is unrestricted. However, the Raman- and IR-active modes are modes at the  $\Gamma$  point of the one-dimensional Brillouin zone of the tube and correspond thus to  $K_{\parallel} = 0$ . Since the points at  $\mu$  and  $2n - \mu$  are equivalent in reciprocal space, all modes of the tube are doubly degenerate, except for the mode that corresponds to  $\mu = 0$  (the  $\Gamma$  point of the sheet) and the mode that corresponds to  $\mu = n$  (the  $M$  point of the sheet). If one applies the strict selection rules according to the  $C_{2nv}$  symmetry group, the modes of the sheet at  $\Gamma$  map onto tube modes with  $A$  symmetry, the modes at  $M$  map onto modes of  $B$  symmetry, and the modes

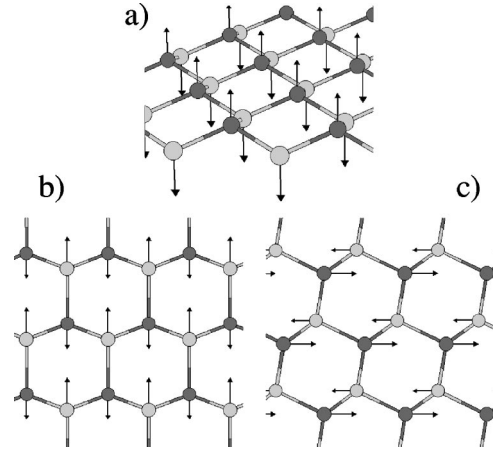


FIG. 6. Sketch of the optical phonon modes at  $\Gamma$  in the hexagonal BN sheet: (a) out-of-plane mode, (b) transverse optical (TO) mode, and (c) longitudinal optical (LO) mode. For the assignment of “transverse” and “longitudinal,” the phonon wave vector points in a horizontal direction with  $q \rightarrow 0$ .

at  $\mu = 1, \dots, n-1$  map onto modes of symmetry  $E_1, \dots, E_{n-1}$ . Since there are six different phonon branches in the sheet, there are six different phonon modes in the tube for each of the above symmetries. Each of the six phonon branches leads to  $n+1$  different phonon modes in the tube,  $(n-1)$   $E$  modes, one  $A$  mode, and one  $B$  mode. Since the  $E$  modes are doubly degenerate, this sums up to  $12n$  phonon modes corresponding to the  $4n$  atoms in the unit cell of a zigzag tube.

Figures 6 and 7 demonstrate the mapping of the three optical modes of the sheet at  $\Gamma$  onto the corresponding  $A$  modes of the tube. The out-of-plane optical (ZO) modes of the sheet lead to radial (R) “buckling” modes of the tube where all boron atoms move inwards (outwards) at the same time and all nitrogen atoms move outwards (inwards), giving rise to an oscillation of the buckling amplitude in the tube. The transverse optical (TO) mode of the sheet maps onto a longitudinal (L) mode of the tube and, accordingly, the longitudinal optical (LO) mode of the sheet maps onto a transverse or tangential (T) mode of the tube. In the  $A$  modes, all

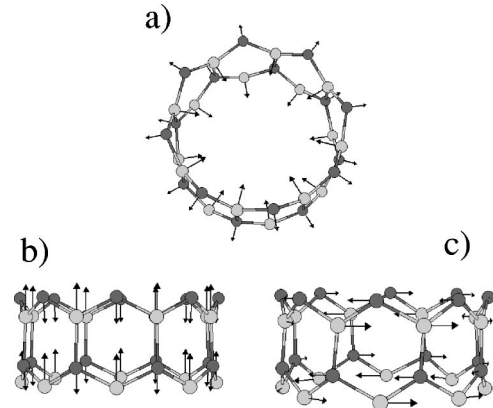


FIG. 7. Sketch of high-frequency  $A$  modes in a BN zigzag tube: (a) radial buckling (R) mode, (b) bond-stretching or longitudinal (L) mode, and (c) bond-bending or tangential (T) mode.



atoms along the circumference move in phase (corresponding to  $K_{\perp}=0$ ). In the modes of  $E_i$  symmetry, there are  $2i$  nodes along the circumference ( $i$  nodal planes containing the symmetry axis of the tube). The  $B$  modes contain  $2n$  nodes along the circumference which means that a rotation by  $\phi/2$  (with the proper translation along the tube axis) maps the mode onto its negative. In other words, for the  $B$  modes, neighboring “columns” of atoms oscillate with a phase difference of  $\pi$ .

The points in the Brillouin zone of the sheet that give rise to the Raman- and IR-active  $A$ ,  $E_1$ , and  $E_2$  modes are denoted in Fig. 5. They are the points at and close to  $\Gamma$ . With larger tube diameter (increasing  $n$ ), the points giving rise to the  $E_1$  and  $E_2$  modes converge towards the  $\Gamma$  point of the BN sheet. Therefore, as a first check on the frequencies of active modes of large diameter tubes, it is sufficient to look at the frequencies at the  $\Gamma$  point of the sheet. The frequencies of modes that correspond to the acoustic branches of the sheet converge accordingly to zero for large diameters. Note that not all of the  $A$ ,  $E_1$ , and  $E_2$  modes may be Raman active, because one still has to distinguish between the different “subsymmetries.” E.g., the TO mode of the sheet at  $\Gamma$  [see Fig. 6(b)] folds into a tube mode of  $A_1$  symmetry [see Fig. 7(b)] and is thus Raman active, whereas the LO mode of the sheet at  $\Gamma$  [see Fig. 6(c)] folds into a mode of  $A_2$  symmetry [see Fig. 7(c)] which changes sign under reflection at a plane that contains the symmetry axis of the tube.

If one uses the lower  $C_{nv}$  point group for the symmetry analysis, the modes that have  $B$  symmetry in the  $C_{2nv}$  group turn into  $A$  modes. Similarly, modes of  $E_{n-1}$  symmetry turn into modes of  $E_1$  symmetry and modes of  $E_{n-2}$  symmetry turn into modes of  $E_2$  symmetry. Thus, in addition to the modes at and close to  $\Gamma$ , some modes at and close to the  $M$  point of the sheet become Raman- and IR-active when the lower point-group symmetry is used which may be required in the case of finite-length tubes.

The zone folding for armchair tubes works in an analogous way to the zone folding for zigzag tubes [see Fig. 5(b)]. The only difference is that the active modes of the tube correspond to a discrete set of modes along the line  $\Gamma \rightarrow M \rightarrow \Gamma$  in the reciprocal space of the sheet. As in the case of the zigzag nanotubes, it is the sheet modes at and close to  $M$  that become active upon using the lower  $C_{nh}$  point group for the symmetry analysis.

Finally, Fig. 5(c) illustrates the zone folding for a general chiral nanotube. In the example, we have chosen a  $(4n,n)$  tube with a relatively short primitive translation vector  $\vec{T}$ . As in the case of armchair and zigzag tubes, the quantization of the circumferential phonon wave vector corresponds in the reciprocal space of the sheet to a discrete set of modes along a line  $\Gamma \rightarrow M \rightarrow \Gamma$ . However, the line does not connect nearest or next-nearest  $\Gamma$  points but connects  $\Gamma$  points farther apart (with the distance depending on the chirality of the tube).

## VII. DIAMETER DEPENDENCE OF RAMAN- AND IR-ACTIVE MODES

In this section we present the results of our *ab initio* calculations of selected zigzag, chiral, and armchair tubes and

compare with the results obtained by zone folding the *ab initio* dispersion relation of the single sheet. The  $C_{2nv}$ ,  $C_{2nh}$ , and  $C_N$  symmetry groups have been used to evaluate the selection rules for the zigzag, armchair, and chiral tubes, respectively. I.e., in structurally perfect and “infinitely” long tubes, only the displayed modes are expected to be active. Figure 8 displays the frequencies of the Raman- and IR-active modes of the three types of tubes as a function of the tube diameter  $D$ . The *ab initio* values are plotted as symbols, while the zone-folding values are connected by lines in order to guide the eye and extrapolate to larger tube diameters. Three frequency regimes are easily distinguishable.

(1) The low-frequency modes whose frequencies approach zero for  $D \rightarrow \infty$  are the modes that are derived from the acoustic branches of the sheet.

(2) The three modes that approach  $\omega \approx 818 \text{ cm}^{-1}$  for  $D \rightarrow \infty$  are radial (R) modes [see Fig. 7(a)] which are related to the optical out-of-plane (ZO) modes [Fig. 6(a)] in the dispersion relation of the sheet (Fig. 2).

(3) The high-frequency regime above  $1200 \text{ cm}^{-1}$  consists of longitudinal (L) and transverse (T) modes [Figs. 7(b) and 7(c)] which are zone-folded TO and LO modes of the sheet [Figs. 6(b) and 6(c)].

We discuss at first the three different frequency regimes separately in the case of the zigzag tubes (left panel of Fig. 8). Afterwards, we extend the discussion to the chiral and armchair tubes.

Figure 9 is a double-logarithmic plot of the low-frequency modes in the zigzag nanotubes. For the RBM (marked by asterisks), we have also included the values of chiral and armchair tubes. From phonon calculations in C nanotubes, it is well known that the RBM is inversely proportional to the tube diameter<sup>25</sup>:  $\omega_{\text{RBM}} \propto 1/D$ . The same holds for BN nanotubes. In fact, not only the RBM, but most of the low-frequency modes display the same  $1/D$  scaling. This can be easily understood from the phonon dispersion of the sheet (Fig. 2) in combination with the zone-folding procedure in Fig. 5: The LA and TA branches of the sheet have a linear slope at the  $\Gamma$  point. The distance between the  $\Gamma$  point and the points that map onto the  $E_1$  and  $E_2$  modes in Fig. 5 is proportional to  $1/N$  (with  $N$  being the number of hexagons in the tube unit cell) and hence proportional to  $1/D$ . Hence, all the low-frequency modes in the tubes that are folded from the LA and TA branches of the sheet exhibit the  $1/D$  scaling. Only the frequency of the lowest  $E_2$  mode in Fig. 9 displays a  $1/D^2$  proportionality.<sup>28</sup> This is because it is folded from the ZA mode of the sheet which does not increase linearly but quadratically around the  $\Gamma$  point.<sup>2</sup> For small diameter, the phonon modes deviate from the functional form  $A/D$  or  $A/D^2$ , because the linear-quadratic behavior in the acoustic branches of the sheet ceases to be valid further away from the  $\Gamma$  point. Only the RBM follows the functional behavior  $A/D$  down to very low radius. In fact, in the case of the RBM, this radius dependence does not follow from the zone-folding picture, but can be proven analytically (see Ref. 25 and the Appendix of this paper).

It is commonly stated that the RBM cannot be obtained with the zone-folding procedure because it is an  $A$  mode and

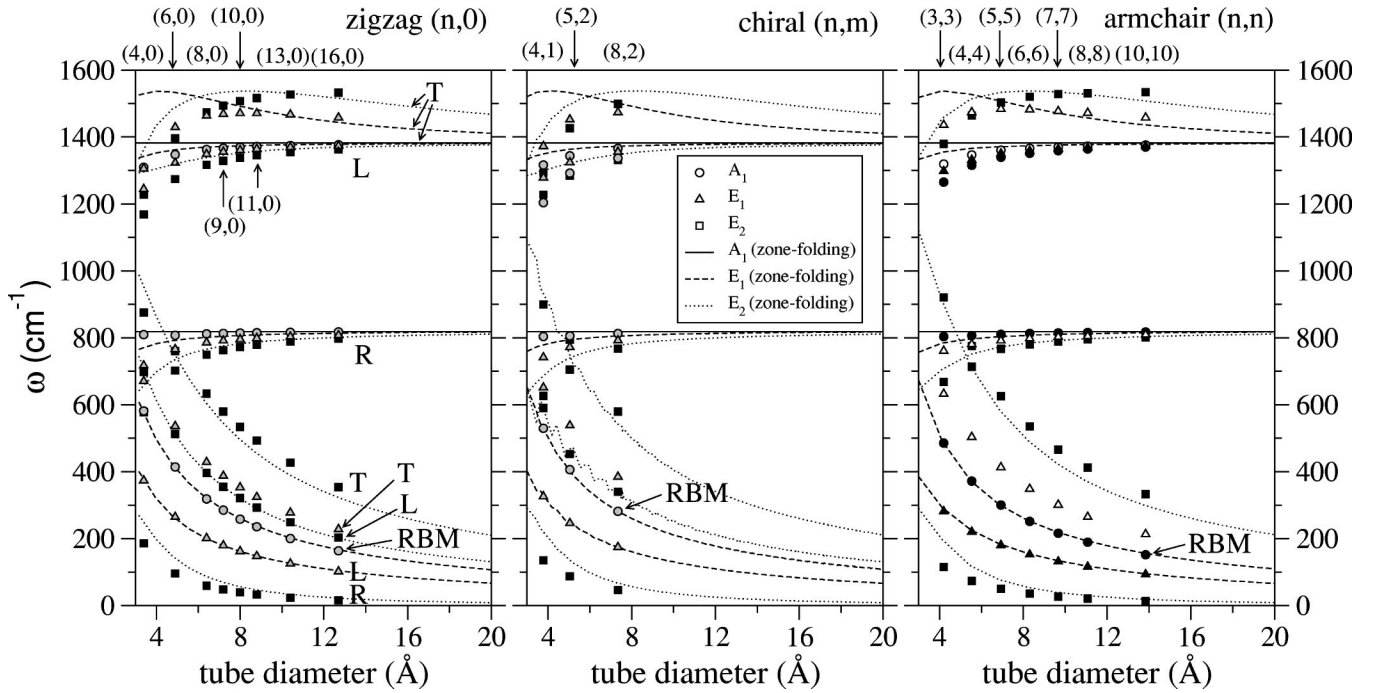


FIG. 8. Frequencies of Raman- and IR-active modes in BN nanotubes as a function of tube diameter: comparison of *ab initio* values (symbols) with zone-folding method (lines). The shape of the symbols denotes the symmetry of the modes (see legend). Black filling marks modes which are Raman active only. White filling stands for IR active only. Gray filling stands for modes which are both Raman and IR active. R, L, and T mark the radial, longitudinal, and tangential high-frequency modes (as in Fig. 7).

the predicted frequency would be zero. Surprisingly, in Fig. 8, the RBM lies exactly on a line obtained by zone folding. However, this is the line of the tangential  $E_1$  mode whose *ab initio* values (gray triangles) are stiffened with respect to the zone-folding values. Similarly, the *ab initio* values of the tangential  $E_2$  mode (black squares) are stiffened with respect to the corresponding zone folding line. While it is true that the RBM cannot be obtained from zone folding of an *infinite* sheet, it is related to the in-plane stretching mode of a sheet

of *finite* width. This relation—which similarly holds for C nanotubes—is discussed in the Appendix where we use the simple analogy of a ring of atoms and a finite linear chain of atoms.

The power-law fit of the RBM scaling in Fig. 9 yields a scaling constant  $A = 515 \pm 2 \text{ cm}^{-1} \text{ Å}$  and may be used for the diameter determination in Raman characterization of BN tubes. As is the general trend of phonons in BN as compared to carbon, this value is considerably lower than the corresponding *ab initio* value  $A_C = 572 \text{ cm}^{-1} \text{ Å}$  for the RBM in carbon nanotubes.<sup>28,32</sup> Since the other low-frequencies modes with  $1/D$  scaling may be used as well for the radius determination, we list in Table I the corresponding scaling constants.

We discuss now the radial phonon modes in the intermediate-frequency regime around  $800 \text{ cm}^{-1}$  [see, e.g., panel (a) of Fig. 8]. According to the zone-folding picture, the A mode should be diameter independent and have con-

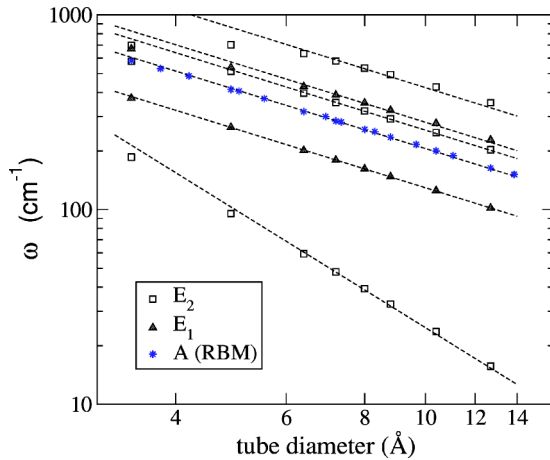


FIG. 9. Double-logarithmic plot of the low phonon frequencies in the BN zigzag tubes. The dashed lines are least-squares fits to the form  $A/D^2$  for the lowest  $E_2$  mode and to the form  $A/D$  for all other modes. The fit has been performed on the diameter interval between  $6 \text{ Å}$  and  $14 \text{ Å}$ .

TABLE I. First-principles determination of scaling constants for the  $A/D$  dependence of the low-frequency modes as a function of the tube diameter  $D$ .

Mode symmetry	$A (\text{cm}^{-1} \text{ Å})$
$E_1$ (L)	324
A (RBM)	515
$E_2$ (L)	640
$E_1$ (T)	702
$E_2$ (T)	1058



stant frequency of  $\approx 818 \text{ cm}^{-1}$ . Indeed, the *ab initio* values lie almost exactly on this line. The  $E_1$  branch is the nearest neighbor in frequency of the  $A$  mode and the  $E_2$  branch is the next-nearest neighbor, because in the zone-folding picture (Fig. 5), the  $E_1$  and  $E_2$  modes derive from the points close to the  $\Gamma$  point of the sheet. Since in the dispersion relation of the BN sheet (Fig. 2) the ZO branch approaches the  $\Gamma$  point from below, the radial  $E_1$  and  $E_2$  modes both have lower frequency than the corresponding  $A$  mode. At small diameters, the *ab initio* values lie below the zone-folding curves due to bond weakening introduced by curvature effects.

The L and T modes of the high-frequency branch converge towards the asymptotic value  $\omega = 1380 \text{ cm}^{-1}$  for  $D \rightarrow \infty$ . In the zone-folding picture, the  $E_1$  and  $E_2$  L modes approach this value from below since in the dispersion relation of the sheet (Fig. 2), the corresponding TO branch from which these modes are derived approach the  $\Gamma$  point from below. The LO branch, in contrast, displays a strong overbending which leads to the nonmonotonic diameter scaling of the  $E_1$  (T) and  $E_2$  (T) modes in Fig. 8. The *ab initio* values follow the general trend of the zone-folding curves. However, all high-frequency T and L modes, even the  $A$  modes which should be diameter independent, experience a strong downshift for small diameter. This general trend is also observed for the C nanotubes<sup>28</sup> and can be attributed to curvature effects. The  $E_1$  (T) mode displays the nonmonotonic behavior which is predicted by zone folding, but due to the curvature-induced softening at small radius, it reaches the maximum at a higher diameter than the zone-folding curve. It is expected that the  $E_2$  (T) mode displays a similar behavior, but since the *ab initio* calculations are restricted in diameter (due to computational feasibility), we can only assume that the  $E_2$  (T) branch will bend down for larger diameter and ultimately converge towards the asymptotic value of  $1380 \text{ cm}^{-1}$ .

The scaling of the phonon frequencies with tube diameter is very similar for zigzag, chiral, and armchair tubes as can be seen from comparing the three panels of Fig. 8. In the case of the chiral tubes, the zone-folding lines of the low-frequency L modes and—to a lesser extent—the ones of the low-frequency T modes display a zigzag pattern. We have calculated all chiral nanotubes in the diameter range between 3 and 20 Å and connected the discrete points by lines in order to guide the eye. For large diameter, the frequencies of the low-frequency modes follow the same scaling as given in Table I for the zigzag tubes. This is because the slope of the acoustic branches of the sheet at  $\Gamma$  is independent of the direction in the Brillouin zone (corresponding to an isotropic sound velocity in all directions). Only at smaller diameter, corresponding to a larger distance from the  $\Gamma$  point in the dispersion relation of the sheet where the LA and TA modes deviate from the linear behavior, does the frequency clearly depend on the chiral angle. The slopes of the zigzag and armchair curves are the limiting cases. E.g., the zone-folding curve of the  $E_2$  (T) mode reaches a value of  $1000 \text{ cm}^{-1}$  at  $D = 3 \text{ Å}$  for the zigzag tubes and a value of  $1150 \text{ cm}^{-1}$  for the armchair tubes.

In Fig. 8, only Raman- or IR-active modes are shown.

This leads to a different number of displayed values in the three different panels as outlined in Sec. V. The fact that for zigzag and chiral tubes the IR-active modes are a subset of the Raman-active modes while for armchair tubes the two sets are disjoint should help in the experimental identification of the ratio of different chiralities in a macroscopic tube sample. In particular, the RBM can be detected both by Raman and IR spectroscopy in zigzag and chiral tubes, while in the case of armchair tubes, it should only appear in the Raman spectrum. Of course, an exact theoretical calculation of the chirality dependence of IR and Raman *intensities* is desirable for this purpose.

## VIII. BUNDLING OF TUBES

So far, we have assumed that the tubes are isolated. I.e., we have chosen a large intertube distance in a periodic array of tubes in order to minimize the effects of intertube interaction on the phonon frequencies. In the produced samples of single-walled BN tubes,<sup>14,23</sup> some tubes are indeed isolated, but many tubes appear in bundles containing on average six to ten tubes. The nonuniform deformation of tubes and the close intertube distance may lead to a modification of some of the phonon frequencies. For carbon nanotubes, the effect of bundling was calculated by a tight-binding method including a Lennard-Jones potential to properly describe the interatomic forces beyond the cutoff radius which is inherent in the tight-binding parametrization.<sup>61–63</sup> In the calculations of Kahn and Lu<sup>61</sup> the effect of bundling does not exceed  $10 \text{ cm}^{-1}$  except for the very-low-energy  $E_1$  and  $E_2$  modes. Interestingly, in their calculations, the low-frequency modes are stiffened while the high-frequency modes are slightly softened. The RBM is stiffened by 10%.<sup>62</sup> In Ref. 63, it was pointed out that due to the intertube interaction, the RBM hybridizes with an  $E_n$  mode, leading to a splitting into two modes. The lower of these two modes is stiffer than the RBM of the isolated tube for small and medium tube radii and is slightly softer for large tube radii.

We investigate the effect of bundling in BN nanotubes by calculating a close-packed (hexagonal) lattice of nanotubes with an intertube distance of 3.7 Å. As in the case of “isolated” tubes, the geometry is optimized. Due to the packing, the tubes acquire a slightly oval form. For the (8,8) tube with a diameter of 11.1 Å, the difference between the long and short axes is 0.04 Å which is about the same magnitude as the buckling distance between B and N atoms for this tube. This slight deviation from the ideal cylindrical symmetry prevents the symmetrization of the dynamical matrix and requires the displacement of all atoms in the unit cell for the calculation of phonon frequencies.

In Table II we compare the (Raman- and IR-active) phonon frequencies of a close-packed (8,8) tube with a (quasi-) isolated (8,8) tube. The general effect of bundling is a splitting of the doubly degenerate  $E$  modes of the isolated tube into two modes with slightly different frequencies. Most phonon modes (except for the lowest  $E_{2g}$  mode) are softened. The effect, however, is weak and does not exceed  $10 \text{ cm}^{-1}$  in most cases. Surprisingly, also the radial breathing  $A_1$  mode and the  $A_1(R)$  buckling mode are slightly soft-

TABLE II. Change of phonon modes due to close packing of BN tubes in a periodic array: Raman- and IR-active modes for an “isolated” BN(8,8) tube (with an intertube distance of 7.4 Å) in comparison with the modes in a “solid of tubes” (intertube distance 3.7 Å). R, L, and T denote radial, longitudinal, and tangential modes (see Fig. 7).

		Isolated BN(8,8)	Close-packed BN(8,8)
$E_{2g}$	R	20.8	7.7/22.7
$E_{1g}$	L	115.7	115.0/115.6
$A_g$	R	189.3	186.9
$E_{1u}$	T	264.7	262.7/263.7
$E_{2g}$	T	412.0	409.6/410.5
$E_{2g}$	R	795.2	791.2/791.5
$E_{1u}$	R	805.0	798.5/798.8
$A_g$	R	815.8	812.8
$A_g$	T	1364.2	1356.8
$E_{1g}$	L	1368.3	1356.0/1356.6
$A_u$	L	1372.0	1360.6
$E_{1u}$	T	1472.1	1424.8/1425.6
$E_{2g}$	T	1530.7	1528.9/1529.1

ened. Apparently, the electrostatic intertube interaction acts, on average, as an attractive force which counteracts the hardening of phonons that would take place if only the repulsion caused by the beginning intertube overlap of the wave functions would modify the frequency. A notable exception to the weak influence of bundling is the  $E_1$  modes [especially the high-frequency  $E_{1u}(T)$  mode] which are more strongly softened than their related  $A$  and  $E_2$  modes of like frequency. The reason for this is the polar nature of BN. In the  $E_1$  modes, at the distance of closest approach between neighboring tubes, equivalent atoms are locally moving as in two parallel planes. This softens the mode and makes it susceptible to LO-TO splitting. Accordingly, in C nanotubes, where the electrostatic interaction is absent, the  $E_1$  modes do not experience a different shift by bundling than the  $A$  and  $E_2$  modes.

## IX. CONCLUSION

We have presented *ab initio* calculations for the lattice dynamics of various BN nanotubes with different diameters and chiralities. In combination with the zone-folding method which allows extrapolation to tubes with higher radii, the calculations offer an accurate tool for the assignment of peaks in experimental Raman and IR spectra.

The lattice dynamics of BN tubes is similar to that of carbon nanotubes. The most important difference is the polarity of the system which leads to softer bonds and lower phonon frequencies. Furthermore, the lower symmetry of BN tubes gives rise to a higher number of Raman- and IR-active modes than in C tubes (provided that in both cases the nonsymmorphic rod groups are used for the selection rules<sup>57,58</sup>).

As for carbon nanotubes, the lattice dynamics of BN nanotubes can be explained to a large extent by the zone-folding method, i.e., the rolling of a single sheet of BN into a tube with quantization of the vibrations along the tube

circumference. The sheet dispersion relation is very similar to that of bulk hexagonal BN.<sup>36</sup> However, the splitting between the longitudinal and transverse optical branches is missing. Instead, the LO branch displays a strong overbending which is much more pronounced than in the phonon dispersion of the single graphene sheet. This strong overbending is responsible for the strongly nonmonotonic diameter scaling of the transverse high-frequency modes in the tubes. The low-frequency modes scale inversely proportionally to the diameter squared as predicted by the zone-folding method. This may serve as an accurate tool for the spectroscopic determination of tube radii. The frequency of the radial breathing mode cannot be deduced from the conventional zone-folding method. However, its frequency can be understood by rolling up a sheet of finite width.

A combined study of BN tubes by Raman and IR spectroscopy can serve to distinguish armchair tubes, where IR- and Raman-active modes are disjoint, from chiral and zigzag tubes, where the IR-active modes are a subset of the Raman-active modes. In particular, the radial breathing mode is both Raman and IR active for chiral and zigzag tubes but only Raman active for armchair nanotubes. We have shown that the effect of bundling on the phonon frequency is low. This justifies the use of the phonon frequencies of isolated tubes for a spectroscopic assignment of macroscopic samples where both isolated and bundled tubes appear.

The present study provides reference data on vibrational properties for future experimental analysis. In particular, it would be very much desirable to perform UV resonant Raman scattering in BN samples in order to obtain higher intensities of the modes and to assess how the resonant and nonresonant Raman spectra are related. This could have also implications for the present understanding of the Raman spectra in C tubes which are always resonant.

## ACKNOWLEDGMENT

This work was supported by the European Community research and training network COMELCAN (Contract No. HPRN-CT-2000-00128), by MCyT Grant No. MAT2001-0946, and by the University of the Basque Country. We acknowledge helpful discussions with Thomas Pichler, Gian-Marco Rignanese, Jean-Christophe Charlier, Ofir Alon, Michele Lazzeri, Francesco Mauri, and Daniel Sánchez-Portal. The calculations were performed on the high-performance computing facilities of the Donostia International Physics Center and the European Center for parallelization of Barcelona (CEPBA).

## APPENDIX: ZONE FOLDING OF THE RADIAL BREATHING MODE

The frequency of the radial breathing mode cannot be obtained from the ordinary zone-folding procedure, because it would be given by the frequency of the acoustic modes of the sheet at the  $\Gamma$  point yielding zero frequency. However, as shown in Fig. 8 the *ab initio* values of the RBM of BN tubes lie exactly on the zone-folding line for the tangential  $E_1$  mode. This behavior is not accidental but can also be ob-

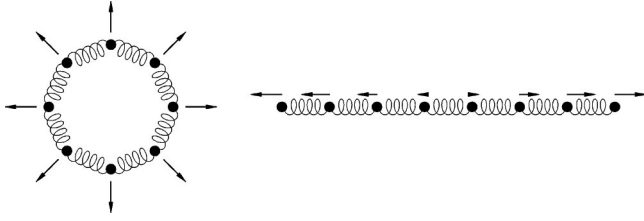


FIG. 10. Schematic model system for the construction of the radial breathing mode: RBM in a ring of atoms and linear stretching mode in a finite linear chain of atoms connected by springs.

served in the case of carbon nanotubes. In this appendix we explain this coincidence with a simple analytical model.

The important point to note is that the RBM cannot be explained from the zone folding of an *infinite* sheet but can be constructed from the in-plane stretching mode of a sheet of *finite* width. Reducing the problem by one dimension, we compare the RBM of a ring of atoms with the linear stretching mode in a finite one-dimensional chain containing  $N$  atoms (see Fig. 10). We assume that the atoms of mass  $M$  are connected by springs of strength  $K$  which only act between nearest neighbors. We follow closely the derivation of the phonon dispersion relation in the infinite monatomic chain of Ref. 64 where Born-von Karman boundary conditions are used; i.e., the atom  $N+n$  coincides with atom  $n$ . If  $u_n$  denotes the deviation of the  $n$ th atom from its equilibrium position, the total harmonic potential can be written as

$$U = \frac{1}{2} K \sum_{n=1}^N (u_{n+1} - u_n)^2. \quad (\text{A1})$$

Assuming a time dependence of  $\exp[i\omega t]$  for all the atoms, this leads to the secular equation

$$M\omega^2 \begin{pmatrix} u_1 \\ \vdots \\ \vdots \\ \vdots \\ \vdots \\ u_n \end{pmatrix} = K \begin{pmatrix} 2 & -1 & 0 & \cdots & 0 & -1 \\ -1 & 2 & -1 & \ddots & & 0 \\ 0 & -1 & \ddots & \ddots & \ddots & \vdots \\ \vdots & \ddots & \ddots & \ddots & -1 & 0 \\ 0 & & \ddots & -1 & 2 & -1 \\ -1 & 0 & \ddots & 0 & -1 & 2 \end{pmatrix} \begin{pmatrix} u_1 \\ \vdots \\ \vdots \\ \vdots \\ \vdots \\ u_n \end{pmatrix}. \quad (\text{A2})$$

For the infinite chain, the eigenvectors are given by

$$u_n(k) = \exp[ikna], \quad (\text{A3})$$

where  $a$  denotes the distance between neighboring atoms and the Born-von Karman boundary conditions require that

$$k = \frac{2\pi m}{a N}, \quad (\text{A4})$$

with  $m=0,1,\dots,N-1$ . The corresponding eigenvalues yield the well-known dispersion relation

$$\omega(k) = 2 \sqrt{\frac{K}{M}} \left| \sin \frac{1}{2} ka \right|. \quad (\text{A5})$$

The mode with  $m=1$ , which in the zone-folding picture should fold onto the  $E_1$  mode whose frequency is “taken” by the RBM, has the frequency

$$\omega_1^{(inf)} = 2 \sqrt{\frac{K}{M}} \left| \sin \frac{\pi}{N} \right| \approx 2 \sqrt{\frac{K}{M}} \frac{\pi}{N}. \quad (\text{A6})$$

For the finite chain, the matrix in Eq. (A2) has the form

$$\begin{pmatrix} 1 & -1 & 0 & \cdots & 0 & 0 \\ -1 & 2 & -1 & \ddots & & 0 \\ 0 & -1 & \ddots & \ddots & \ddots & \vdots \\ \vdots & \ddots & \ddots & \ddots & -1 & 0 \\ 0 & & \ddots & -1 & 2 & -1 \\ 0 & 0 & \ddots & 0 & -1 & 1 \end{pmatrix}; \quad (\text{A7})$$

i.e., the coupling of atom 1 to atom  $n$  is suppressed. However, if the chain is very long, the influence of the open end is not very strong and matrix (A7) can be approximated by the one of Eq. (A2). With this approximation, we obtain the same eigenvectors as for the infinite chain [Eq. (A3)]; however, the open ends lead to the condition

$$k = \frac{\pi m}{a N}, \quad (\text{A8})$$

with  $m=0,1,\dots,N-1$ , as opposed to Eq. (A4). For the linear stretching mode which we suggest as a candidate for folding onto the RBM of the ring,  $m=1$ , and

$$\omega_1^{(fin)} = 2 \sqrt{\frac{K}{M}} \left| \sin \frac{\pi}{2N} \right| \approx \sqrt{\frac{K}{M}} \frac{\pi}{N}. \quad (\text{A9})$$

For the ring of atoms connected by nearest-neighbor springs, it is considerably more complex to write down the secular equation, because the system is intrinsically two-dimensional, corresponding to tangential and radial displacements of the atoms. However, for the case of the RBM, where all the atoms are moving in radial direction, the problem reduces to one dimension. When all the atoms are displaced by  $\delta r$ , the displacement difference between two neighboring atoms in Eq. (A1) equals the elongation of the circumference divided by the number of atoms,  $N$ ,

$$u_{n+1} - u_n = \frac{2\pi}{N} dr, \quad (\text{A10})$$

and the harmonic potential is



$$U(\delta r) = \frac{1}{2}KN\left(\frac{2\pi}{N}\right)^2\delta r^2. \quad (\text{A11})$$

Newton's equation of motion yields then immediately the frequency

$$\omega_{RBM} = \sqrt{\frac{K}{M}} \frac{2\pi}{N} = \sqrt{\frac{K}{M}} \frac{a}{r}. \quad (\text{A12})$$

An analogous equation was originally derived by Jishi *et al.*<sup>25</sup> in order to prove the  $1/r$  scaling of the RBM frequency in C nanotubes. This was done within a force-constant model that takes up to fourth-nearest-neighbor interaction into account. Equation (A12) corresponds to the nearest-neighbor interaction term of Eq. (7) in Ref. 25. The  $1/r$  scaling does not depend on the range of atom-atom interactions to be included (*ab initio* calculations yield the same scaling). For this reason we use the simple nearest-neighbor-interaction-only model in order to highlight the connection of RBM and line-stretching modes.

Note the equality  $\omega_{RBM} = \omega_1^{(inf)} = 2\omega_1^{(fin)}$ . The second equality states that while the linear stretching mode of the open chain folds onto the RBM of the ring, its frequency is doubled. Instead, the frequency of the RBM coincides with the frequency of the first longitudinal mode in the *infinite* chain (which has two nodes per  $N$  atom unit cell and coincides with the second longitudinal mode in the finite chain). However, in the usual zone-folding procedure, the latter

mode should fold onto the tangential  $E_1$  mode of the ring, which also contains two nodes along the circumference. The calculations of the tube (see Fig. 8) and also a numerical solution of the frequencies of the  $N$ -atom ring show that the  $E_1$  mode is stiffened considerably with respect to the zone-folding value. Similarly, the tangential  $E_2$  mode with four nodes along the circumference is stiffened with respect to the zone-folding value which is the frequency of the second (fourth) longitudinal mode infinite (finite) chain, respectively. It is important to note that this stiffening is not a curvature effect, i.e., not due to the modification of the bond strength due to an admixture of  $sp^3$  hybridization to the  $sp^2$  bonds of the sheet. This possibility can be ruled out because the stiffening persists for large tube radii and the stiffening is also present in the ring model where the interaction of nearest neighbors is described by a simple spring irrespectively of the curvature of the system. While we could not find a simple analytical formula for the amount of stiffening we deduce that it is due to the coupling of tangential and radial motion when the in-line (in-plane) modes of the chain (sheet) are mapped into the corresponding modes of a ring (tube). In contrast, the frequency of the out-of-plane modes of the sheet match almost perfectly the frequencies of the corresponding modes in the tubes. In this case, the out-of-plane motion translates directly into a radial motion. The remaining discrepancies in the frequencies for small tubes can safely be assigned to curvature effects.

- 
- <sup>1</sup>S. Iijima, *Nature* (London) **354**, 56 (1991).  
<sup>2</sup>R. Saito, G. Dresselhaus, and M.S. Dresselhaus, *Physical Properties of Carbon Nanotubes* (Imperial College Press, London, 1998).  
<sup>3</sup>*Carbon Nanotubes: Synthesis, structure, properties, and applications*, edited by M.S. Dresselhaus, G. Dresselhaus, and Ph. Avouris (Springer-Verlag, Berlin, 2001).  
<sup>4</sup>A. Rubio, J.L. Corkill, and M.L. Cohen, *Phys. Rev. B* **49**, 5081 (1994).  
<sup>5</sup>X. Blase, A. Rubio, S.G. Louie, and M.L. Cohen, *Europhys. Lett.* **28**, 335 (1994).  
<sup>6</sup>N.G. Chopra, J. Luyken, K. Cherry, V.H. Crespi, M.L. Cohen, S.G. Louie, and A. Zettl, *Science* **269**, 966 (1995).  
<sup>7</sup>A. Loiseau, F. Willaime, N. Demoncy, G. Hug, and H. Pascard, *Phys. Rev. Lett.* **76**, 4737 (1996).  
<sup>8</sup>D.P. Yu, X.S. Sun, C.S. Lee, I. Bello, S.T. Lee, H.D. Gu, K.M. Leung, G.W. Zhou, Z.F. Dong, and Z. Zhang, *Appl. Phys. Lett.* **72**, 1966 (1998).  
<sup>9</sup>D. Goldberg, Y. Bando, W. Han, K. Kurashima, and T. Sato, *Chem. Phys. Lett.* **308**, 337 (1999).  
<sup>10</sup>Y. Chen, J.F. Gerald, J.S. Williams, and S. Bulcock, *Chem. Phys. Lett.* **299**, 260 (1999).  
<sup>11</sup>J. Cummings and A. Zettl, *Chem. Phys. Lett.* **316**, 211 (2000).  
<sup>12</sup>T. Laude, Y. Matsui, A. Marraud, and B. Jouffrey, *Appl. Phys. Lett.* **76**, 3239 (2000).  
<sup>13</sup>E. Bengu and L.D. Marks, *Phys. Rev. Lett.* **86**, 2385 (2001).  
<sup>14</sup>R.S. Lee, J. Gavillet, M. Lamy de la Chapelle, A. Loiseau, J.-L. Cochon, D. Pigache, J. Thibault, and F. Willaime, *Phys. Rev. B* **64**, 121405(R) (2001).  
<sup>15</sup>X. Blase, A. Rubio, S.G. Louie, and M.L. Cohen, *Phys. Rev. B* **51**, 6868 (1995).  
<sup>16</sup>E.J. Mele and P. Kral, *Phys. Rev. Lett.* **88**, 056803 (2002).  
<sup>17</sup>A. Rubio, Y. Miyamoto, X. Blase, M.L. Cohen, and S.G. Louie, *Phys. Rev. B* **53**, 4023 (1996).  
<sup>18</sup>P.C. Eklund, J.M. Holden, and R.A. Jishi, *Carbon* **33**, 959 (1995).  
<sup>19</sup>J. Kastner, T. Pichler, H. Kuzmany, S. Curran, W. Blau, D.N. Weldon, M. Delamesiere, S. Draper, and H. Zandbergen, *Chem. Phys. Lett.* **221**, 53 (1994).  
<sup>20</sup>A.M. Rao, E. Richter, S. Bandow, B. Chase, P.C. Eklund, K.A. Williams, S. Fang, K.R. Subbaswamy, M. Menon, A. Thess, R.E. Smalley, G. Dresselhaus, and M.S. Dresselhaus, *Science* **275**, 187 (1997).  
<sup>21</sup>R. Saito, T. Takeya, T. Kimura, G. Dresselhaus, and M.S. Dresselhaus, *Phys. Rev. B* **57**, 4145 (1998).  
<sup>22</sup>U. Kuhlmann, H. Jontoljak, N. Pfänder, P. Bernier, C. Journet, and C. Thomsen, *Chem. Phys. Lett.* **294**, 237 (1998).  
<sup>23</sup>R. Arenal de la Concha, L. Wirtz, J.-Y. Mevellec, S. Lefrant, A. Loiseau, and A. Rubio (unpublished).  
<sup>24</sup>E. Borowiak-Palen, T. Pichler, G.G. Fuentes, B. Bendjemil, X. Liu, A. Graff, G. Behr, R.J. Kalenczuk, M. Knupfer, and J. Fink, *Chem. Commun. (Cambridge)* **2003**, 82.  
<sup>25</sup>R.A. Jishi, L. Venkataraman, M.S. Dresselhaus, and G. Dresselhaus, *Chem. Phys. Lett.* **209**, 77 (1993).  
<sup>26</sup>G. Kresse, J. Furthmüller, and J. Hafner, *Europhys. Lett.* **32**, 729 (1995).

- <sup>27</sup>P. Pavone, R. Bauer, K. Karch, O. Schütt, S. Vent, W. Windl, D. Strauch, S. Baroni, and S. de Gironcoli, *Physica B* **219 & 220**, 439 (1996).
- <sup>28</sup>O. Dubay and G. Kresse, *Phys. Rev. B* **67**, 035401 (2003).
- <sup>29</sup>J. Yu, R.K. Kalia, and P. Vashishta, *J. Chem. Phys.* **103**, 6697 (1995).
- <sup>30</sup>D. Sánchez-Portal, E. Artacho, J.M. Soler, A. Rubio, and P. Ordejón, *Phys. Rev. B* **59**, 12 678 (1999).
- <sup>31</sup>S. Reich, C. Thomsen, and P. Ordejón, *Phys. Rev. B* **64**, 195416 (2001).
- <sup>32</sup>J. Kürti, G. Kresse, and H. Kuzmany, *Phys. Rev. B* **58**, R8869 (1998).
- <sup>33</sup>O. Dubay, G. Kresse, and H. Kuzmany, *Phys. Rev. Lett.* **88**, 235506 (2002).
- <sup>34</sup>D. Sánchez-Portal and E. Hernández, *Phys. Rev. B* **66**, 235415 (2002).
- <sup>35</sup>V.N. Popov, *Phys. Rev. B* **67**, 085408 (2003).
- <sup>36</sup>G. Kern, G. Kresse, and J. Hafner, *Phys. Rev. B* **59**, 8551 (1999).
- <sup>37</sup>The ABINIT code is a common project of the Université Catholique de Louvain, Corning Incorporated, and other contributors (URL: <http://www.abinit.org>).
- <sup>38</sup>W. Kohn and L.J. Sham, *Phys. Rev.* **140**, A1133 (1965).
- <sup>39</sup>J.P. Perdew and A. Zunger, *Phys. Rev. B* **23**, 5048 (1981).
- <sup>40</sup>N. Troullier and J.L. Martins, *Phys. Rev. B* **43**, 1993 (1991).
- <sup>41</sup>S. Baroni, S. de Gironcoli, A. Dal Corso, and P. Giannozzi, *Rev. Mod. Phys.* **73**, 515 (2001).
- <sup>42</sup>X. Gonze, *Phys. Rev. B* **55**, 10 337 (1997); X. Gonze and C. Lee, *ibid.* **55**, 10 355 (1997).
- <sup>43</sup>V.N. Popov, V.E. Van Doren, and M. Balkanski, *Phys. Rev. B* **59**, 8355 (1999).
- <sup>44</sup>The deviation from the cylindrical geometry is relevant for BN tubes packed in a triangular lattice ("tube bundle"). In that case, all elements of the dynamical matrix have to be calculated explicitly.
- <sup>45</sup>L. Wirtz and A. Rubio, *Proc. SPIE* **5118**, 354 (2003).
- <sup>46</sup>*Semiconductors—Basic Data*, edited by O. Madelung (Springer-Verlag, Berlin, 1996).
- <sup>47</sup>This agreement is a nice documentation that the different plane-wave DFT codes yield the same phonon frequencies. Our calculations are done with the code ABINIT (Ref. 37) using Troullier-Martins pseudopotentials (Ref. 40). Phonons are calculated using density functional perturbation theory. Dubay and Kresse (Ref. 28) used the Vienna *ab initio* simulation package (VASP) (Ref. 48) with the projector augmented-wave (PAW) method (Ref. 49) for the electron-ion interaction. Phonons are determined by displacing the atoms within the unit cell and calculating the force constants by the central difference method.
- <sup>48</sup>G. Kresse and J. Hafner, *Phys. Rev. B* **48**, 13 115 (1993).
- <sup>49</sup>P.E. Blöchl, *Phys. Rev. B* **50**, 17 953 (1994).
- <sup>50</sup>C. Oshima, T. Aizawa, R. Souda, Y. Ishizawa, and Y. Sumiyoshi, *Solid State Commun.* **65**, 1601 (1988).
- <sup>51</sup>S. Siebentritt, R. Pues, K.-H. Rieder, and A.M. Shikin, *Phys. Rev. B* **55**, 7927 (1997).
- <sup>52</sup>E. Rokuta, Y. Hasegawa, K. Suzuki, Y. Gamou, C. Oshima, and A. Nagashima, *Phys. Rev. Lett.* **79**, 4609 (1997).
- <sup>53</sup>Y. Miyamoto, M.L. Cohen, and S.G. Louie, *Phys. Rev. B* **52**, 14 971 (1995).
- <sup>54</sup>J. von Neumann and E. Wigner, *Phys. Z.* **30**, 467 (1929).
- <sup>55</sup>The selection rules for Raman and IR spectroscopy are discussed in many textbooks. E.g., a nice introduction can be found in D.C. Harris and M.D. Bertolucci, *Symmetry and Spectroscopy: an Introduction to Vibrational and Electronic Spectroscopy* (Dover, New York, 1989).
- <sup>56</sup>M. Damjanović, T. Vuković, I. Milošević, and B. Nikolić, *Acta Crystallogr., Sect. A: Found. Crystallogr.* **57**, 304 (2001).
- <sup>57</sup>O.E. Alon, *Phys. Rev. B* **63**, 201403 (2001).
- <sup>58</sup>O.E. Alon, *Phys. Rev. B* **64**, 153408 (2001).
- <sup>59</sup>The fact that for zigzag and chiral tubes, the IR-active modes are a subset of the Raman-active modes is different in BN tubes and C tubes and is due to the reduced symmetry (=less strict selection rules) for BN tubes. In carbon tubes, only the set of IR-active modes of chiral tubes partially overlaps with the set of Raman-active modes (Ref. 57). For zigzag and armchair C tubes, the sets of Raman- and IR-active modes are disjoint.
- <sup>60</sup>Since there is no inversion symmetry in the  $C_{nh}$  symmetry group for odd  $n$ , the assignment of modes is different. This does, however, not change the total number of active modes and their distribution: 19 Raman-active modes ( $7A'$ ,  $4E'_1$ ,  $8E'_2$ ) and 10 IR-active modes ( $3A''$  and  $7E'_1$ ).
- <sup>61</sup>D. Kahn and J.P. Lu, *Phys. Rev. B* **60**, 6535 (1999).
- <sup>62</sup>L. Henrard, E. Hernández, P. Bernier, and A. Rubio, *Phys. Rev. B* **60**, 8521 (1999).
- <sup>63</sup>V.N. Popov and L. Henrard, *Phys. Rev. B* **63**, 233407 (2001); L. Henrard, V.N. Popov, and A. Rubio, *ibid.* **64**, 205403 (2001).
- <sup>64</sup>N.W. Ashcroft and N.D. Mermin, *Solid State Physics* (Saunders College Publishing, Orlando, FL, 1976).